Harnessing optogenetics to probe sub-cellular mechanics

Patrick W. Oakes[1,4*], Elizabeth Wagner[2*], Christoph A. Brand[3+], Dimitri Probst[3+], Marco Linke[3+], Ulrich S. Schwarz[3*], Michael Glotzer[2*], Margaret L. Gardel[1*]

[1]Institute for Biophysical Dynamics, James Franck Institute and the Department of Physics, University of Chicago, Chicago, IL 606037

[2]Department of Molecular Genetics and Cell Biology, University of Chicago, Chicago, IL 60637

[3]Institute for Theoretical Physics and BioQuant, Heidelberg University, Heidelberg, Germany

[4]Department of Physics & Astronomy, and Department of Biology, University of Rochester, Rochester, NY 14627

[*,+]Contributed equally

*Corresponding Authors

Abstract

The mechanics of the actin cytoskeleton regulates cell morphogenesis during essential physiological processes. However, the spatially heterogeneous and dynamic nature of the actin cytoskeleton make mechanical measurements and modeling challenging. Here we develop a new approach to probe the mechanics of the contractile actin cytoskeleton by integrating optogenetic control of RhoA, live cell imaging and traction force microscopy. Local activation of RhoA stimulates local contraction, leading to increased traction forces that rapidly propagate across the cell via stress fibers and drive actin flow towards the region of heightened RhoA. Surprisingly, the flow reverses direction when local RhoA activation stops. These experimental data are used to constrain a physical model, which demonstrates that stress fibers are elastic-like, even at time scales exceeding turnover of constituent proteins. We identify zyxin as a regulator of stress fiber mechanics, as they are fluid-like in its absence. Such molecular control of actin mechanics likely plays critical roles in regulation of morphogenic events.

Introduction

A diverse array of essential physiological processes, ranging from the subcellular to the multicellular, depend on the spatial and temporal regulation of contractile forces[1-4]. This regulation drives changes in cell shape[5,6] and mediates interactions with the extracellular environment [7,8]. Changes in contractility can furthermore alter gene expression[9] and impact development[10,11]. The molecular machinery required for generating contractile forces is well conserved and dominated by the actin cytoskeleton, myosin II activity and associated regulatory proteins[4,12,13]. Specifically, actin filaments dynamically organize into distinct contractile architectures, including the cortex and stress fibers [14,15]. Contractile forces are transmitted across the cell by actin arrays and are ultimately to the extracellular matrix by focal adhesions[12,13,16,17].

The regulation of cellular force transmission is controlled by the mechanical properties of actomyosin assemblies. Cellular mechanics has been explored extensively both experimentally[14,18-20] and theoretically[21-23]. Current understanding is that, at time scales comparable to those of typical kinetic processes, the actin cytoskeleton behaves like an elastic solid. Such elasticity enables rapid force transmission across the cell and reversible deformations to preserve cytoskeletal architecture. In contrast, at longer time scales, it is thought dynamic processes make the cytoskeleton predominately like a viscous fluid. Such viscosity enables cytoskeletal flows and remodeling. However, the molecular regulation of cell mechanics is not well understood.

Cellular contractility is largely controlled by the activity of the small GTPase RhoA[24,25], which in adherent cells is preferentially active at the cell periphery[26,27]. RhoA regulates contractility through the promotion of actin polymerization and myosin light chain phosphorylation via the downstream effectors Diaphanous-related formins and Rho-associated Kinase (ROCK), respectively. RhoA activity is required for stress fibers and focal adhesions[24,25]. Little, however, is known about how small changes in activity can regulate cell contractility, actin architecture and adhesion.

In this paper, we have used an optogenetic probe to locally activate RhoA in adherent fibroblasts. Plasma membrane recruitment of the RhoA specific guanine exchange factor (GEF) LARG induces local

42 RhoA activation[6,28-30]. Local activation of RhoA leads to an increase in actin polymerization and myosin
43 activity in the region of activation, but it does not stimulate *de novo* stress fiber formation or changes
44 in focal adhesion morphology. We find that exogenous RhoA activation leads to an immediate increase
45 in both the local and global contractility of the cell, followed by a rapid relaxation after GEF
46 recruitment is stopped. The local increase in stress fiber contractility drives an actomyosin flow
47 towards regions of increased RhoA activity. Surprisingly, these flows reverse direction as soon as GEF
48 recruitment ceases. Using physical modeling, we show this behavior is consistent with stress fibers
49 behaving as predominately elastic-like over hour time scales. We find that zyxin is necessary for this
50 elasticity; in its absence, stress fibers become predominately fluid-like even at second time scales.
51 These results suggest that stress fiber mechanics is sensitive to small changes in composition, which
52 has significant implications for regulation of force transmission and cytoskeletal organization.
53
54 **Results**
55 **Spatiotemporal control of RhoA and its downstream effectors**
56 To spatially and temporally control contractility in adherent cells, we adapted a previously established
57 optogenetic probe[6,28] to act on the RhoA signaling pathway (Figure 1a). During stimulation by blue
58 light, a cytosolic fusion protein, photo-recruitable GEF (prGEF), consisting of tandem PDZ domains
59 fused to the DH domain of the RhoA specific GEF LARG[6], is recruited to the plasma membrane where it
60 activates RhoA (Figure 1b). To illustrate the local recruitment of prGEF we tagged it with the
61 fluorophore mCherry and imaged an NIH 3T3 fibroblast expressing the constructs on a glass coverslip
62 (Figure 1c). A digital micromirror device was used to spatially control the illumination of the blue
63 activating light (orange box, Figure 1c), and was pulsed before each image acquisition during the
64 recruitment period. Recruitment of the prGEF to the activation region was rapid and reversible upon
65 extinguishing the stimulating blue light (Figure 1c,d and Supplementary Movie 1).
66
67 To investigate whether recruitment of the prGEF resulted in activity of proteins downstream of RhoA,
68 we tracked the dynamics of actin and myosin light chain (MLC) during recruitment (Figure 1e,g). Both
69 actin and myosin accumulated in the activation regions, resulting in an increase in fluorescence
70 intensity during the 15 min activation period (Figure 1e-h and Supplementary Movies 2-3).

71 Interestingly, local activation of RhoA did not lead to *de novo* stress fiber assembly in the activation
72 region (Figure 1e and Supplementary Movie 2). At the end of the activation period, fluorescence
73 intensities of both actin and myosin returned to baseline levels. These results indicate that exogenous
74 RhoA activation via LARG recruitment is not sufficient to maintain elevated RhoA activity and the
75 concomitant increases in local actin and myosin concentrations. To confirm that local activation of
76 RhoA was acting on actin and myosin through its downstream effectors, formin and ROCK, the
77 experiments were repeated in the presence of either SMIFH2, a pan formin inhibitor[31], or Y-27632, a
78 Rho-associated Kinase inhibitor. Local recruitment of actin and MLC were significantly inhibited by the
79 presence of SMIFH2 and Y-27632, respectively. These results illustrate that RhoA activity and
80 recruitment of its downstream effectors can be spatially and temporally controlled via light.
81
82 **Focal adhesion dynamics and morphology are unperturbed by local increases in RhoA activity**
83 Previous work has suggested that focal adhesion formation and maturation are tension dependent
84 processes driven by increased RhoA activity at adhesion sites [24,25,32]. To test these hypotheses we
85 examined how local RhoA activation affected traction forces and focal adhesions. Cells expressing
86 mCherry-vinculin, a marker of focal adhesions, were plated on polyacrylamide gels coated with
87 fibronectin and traction stresses were measured via Traction Force Microscopy (Figure 2a,b and
88 Supplementary Movie 4)[33,34]. During local activation of RhoA, traction stresses increased at focal
89 adhesion sites, on a similar timescale to that of myosin localization (Figure 1g). Despite the increased
90 force, the total number of adhesions remained essentially constant (Figure 2c). Individual adhesion
91 morphology and vinculin intensity were also unaffected, despite large increases in stress at a majority
92 of previously established adhesion sites during local RhoA activation (Figure 2d & Supplementary
93 Figure S1). Too much RhoA activation, however, results in adhesion failure and detachment from the
94 substrate (Supplementary Figure S2). These result are consistent with previous results that tension
95 alone is not sufficient to drive changes in focal adhesion size[35].
96
97 To determine the effect of local RhoA activation on the overall contractility of the cell, we used traction
98 force microscopy to measure the total strain energy, which reflects the amount of mechanical work
99 done by the cell on its environment[36]. Activation induced a rapid increase in both traction stresses and

strain energy (Figure 2b,c) At the end of the activation period, the strain energy decreased to their original baseline values (Figure 2c). Interestingly, traction stresses were mostly seen to increase at the cell periphery, where traction stresses were already established, and in areas immediately adjacent to the activation region. No change was seen in the activation area itself (Figure 2b). This suggests that locally generated forces balance within the activation region and only unbalanced forces at the edge of this region are turned into productive traction forces. Thus, a local increase of tension leads to globally distributed traction forces at pre-existing focal adhesions.

Cells maintain a contractile set point

That cells return to a similar baseline contractility following a period of exogenous RhoA activation is consistent with previously established ideas of tensional homeostasis[36-38]. To explicitly probe this behavior, we performed a series of local activations of different sizes on a single cell (Figure 2e and Supplementary Movie 5). After measuring the strain energy at an initial steady state, a cell was exposed to three 15 min periods of local RhoA activation of increasing size with relaxation periods between each activation (Figure 2e,f). The strain energy increased concomitant with the size of the activation region. During activation, both local stresses immediately surrounding the activation region, and long-range stresses at the cell periphery could be seen to increase (Figure 2e). Following each activation, the strain energy returned to the initial baseline level (Figure 2f).

To elucidate the underlying mechanical principles, we built a physical model that would capture this physical response. We constructed a continuum model of the cell as a contractile element in series with a viscous and an elastic element (Figure 2g). Contractility was assumed to increase with an exponentially plateauing ramp in the activated region, consistent with the observed accumulation profiles for actin and myosin (Figure 1g), and the substrate was represented as an elastic spring coupled to the cell by a friction element. The model parameters for the elastic modulus, viscosity, friction and contractility were found by fitting the model to the strain energy data, while the value of the substrate stiffness was fixed. This procedure resulted in a curve in good agreement with the experimental data (Figure 2f).

129 We find that both the viscous and elastic elements are necessary to accurately capture the behavior of
130 the system. The ratio of viscosity (~7*10^6 Pa*s) to elasticity (~2*10^3 Pa) defines a viscoelastic
131 relaxation time of approximately 50 minutes; this time scale determines the transition from when the
132 cytoskeleton behaves predominately elastic-like (< 50 min) to predominately fluid-like (> 50 min). Our
133 results thus indicate that stress fibers are predominantly elastic on the scale of tens of minutes, despite
134 proteins within the stress fiber turning over on timescales of tens of seconds[15]. This strong elastic
135 behavior is also consistent with the immediate increase in cell traction stresses at the cell periphery
136 (Figure 2b,e) upon local activation of RhoA in the center of the cell.
137
138 **Stress fibers contract independent of the background network**
139 To investigate the cytoskeletal architectures that give rise to this strong contractility, we tracked
140 myosin dynamics during local RhoA activation. In the steady state, as new actomyosin is polymerized
141 and incorporated into stress fibers, there is a retrograde flow of actomoysin from the periphery
142 towards the cell center[15,17]. Using particle image velocimetry (PIV)[39,40] we measured both the local
143 direction and magnitude of myosin flow. We found that myosin flow rates along the stress fiber
144 increased as myosin accumulated in the activation region creating a local contraction, and that this
145 flow was directed along the orientation of the stress fibers spanning the activation region (Figure 3a,b,
146 Supplementary Figure S3, and Supplementary Movie 6). The flow direction was independent of the
147 activation region geometry, with the direction always being determined by the stress fiber orientation
148 (Supplementary Movie 7).
149
150 The cytoskeleton of a strongly adherent cell is typically thought to be a 2D material comprised of stress
151 fibers embedded in an isotropic cortex[34,41,42]. Since flows induced by local RhoA activation appear to
152 track the orientation of the stress fibers (Figs. 3a,b and S2), we sought to address the relative
153 contractile contributions of the stress fibers and the actin networks. We therefore built a 2D discrete
154 model analogous to the 1D continuum model described above (Figure 3c). The model consists of a
155 triangular mesh with the same contractile, viscous and elastic elements connected in series, with lines
156 of increased contractility representing the stress fibers. Using a simple rectangular cell, we first verified
157 that, without stress fibers, this model recapitulates the results from the one-dimensional continuum

158 model (Figure 3d). Similar to the 1D model above, the contractile components in a region in the center
159 of the cell were slowly increased with an exponentially plateauing ramp. The parameters were then
160 adjusted so that the model both qualitatively and quantitatively recapitulated the expected flow
161 patterns of the 1D continuum model (Figure 3d).
162
163 To explore the relative contributions of the background mesh and the stress fibers, we considered two
164 test cases: (1) If both the mesh and the stress fibers contained contractile elements, the stress fibers
165 pinched inward transverse to their orientation during local activation (Figure 3e); and (2) when
166 contractile elements were only included in the stress fibers, the cytoskeletal flow was restricted to
167 directions along the stress fiber (Figure 3f), consistent with our experimental results (Figure 3a-b,
168 Supplementary Figure S3, and Supplementary Movies 6-7). Since transverse deformations were never
169 seen in experiments, it is clear that the stress fibers must be the predominant contractile elements
170 observable at this resolution which respond to local RhoA-induced contractions. Furthermore, this
171 result illustrates that it is appropriate to think of a stress fiber as a one-dimensional contractile
172 element with viscous and elastic components embedded in a passive viscoelastic network.
173
174 **Stress fibers flow in response to local strain induced by RhoA activation**
175 Having identified the stress fiber as the main contractile unit responding to exogenous RhoA activation,
176 we next sought to address whether stress fibers undergo deformation during contraction. Since stress
177 fibers can be considered as 1D structures, we analyzed myosin flow along the fiber using kymographs.
178 A kymograph drawn along a single stress fiber illustrates that myosin puncta flowed from both ends
179 towards the activation regions when RhoA was activated locally (Figure 4a-b, Supplementary Figure
180 S5). Similarly, a kymograph drawn by projecting the flow speed along the stress fiber from the velocity
181 field created by our PIV analysis illustrates even more clearly how cytoskeletal flow was perturbed by
182 local RhoA activation. Flow of myosin from both ends of the stress fiber reoriented towards the
183 recruitment regions and increased from ~1 nm/s on average to more than 3 nm/s during activation
184 (Figure 4c and Supplementary Figure S5). Strikingly, the flow was also seen to reverse direction, flowing
185 away from the recruitment region and towards the cell periphery, during the relaxation period
186 following the local activation (Figure 4b,c). This flow reversal is reminiscent of the restoring force in

elastic objects that restores its original shape after removal of external force (e.g. recoil of an elastic band after stretch).

We next developed a protocol to measure the magnitude of the stress fiber displacement during these periods of contraction and relaxation (Figure 4d). The displacement in a given fiber was determined by measuring the relative position of puncta along the fiber following 15 minutes of local RhoA activation and 15 minutes after it ceased. During contraction, puncta on either side of the activation region contracted on average ~3 µm from their original position before relaxing back to ~1 µm from their original position (Figure 4d). The relaxation response across many stress fibers from multiple cells could be further clustered into two groups, one which exhibited strong reversal (~80% of the original position) and one which exhibited little to no reversal (~25% of the original position) (Figure 4d).

To determine whether stress fibers were stretching due to the local contraction, we used cells expressing mApple-α-actinin, an actin crosslinker which localizes to well defined puncta on stress fibers (Figure 4e and Supplementary Movie 8). We created kymographs of α-actinin flow during local activation of RhoA and tracked paths of individual puncta (Figure 4f). The velocity of individual puncta was determined from the slope of the tracks in the kymograph and plotted as a function of distance from the activation zone (Figure 4g). Puncta along the stress fiber moved at similar speeds, indicating that, in general, the stress fiber was translating as a rigid rod during the local contraction (Figure 4g). Where present, changes in velocity between neighboring puncta were abrupt (blue arrow Fig 4g), suggesting points of structural failure along a fiber. These results indicate that the strain induced in the stress fiber is restricted to the local contraction in the activation region and discrete sites of extension in regions outside the activation region.

By fitting the experimental kymographs to both our 1D continuum and 2D discrete models, we show that similar flow patterns emerge naturally from the mechanics of the system (Figure 4h). The high elasticity of the stress fiber, specifically the ratio of elasticity to viscosity, is sufficient to recapitulate the flow profiles that were seen during both RhoA activation and relaxation. Furthermore, the

215 parameters found from the kymograph fitting process were consistent with the parameter values
216 found when fitting the strain energy (Table 2).
217
218 **Zyxin is recruited to sites of extension and compression on stress fibers**
219 In order to probe the underlying molecular basis of this elasticity, we sought to identify stress fiber-
220 associated proteins that could contribute to the recoil behavior. Zyxin has been previously established
221 as a mechanosensitive protein that dynamically localizes to sites of strain along stress fibers[43,44], in
222 addition to focal adhesions[45]. Using cells expressing mCherry-zyxin, we monitored zyxin activity during
223 RhoA activation (Figure 5a and Supplementary Movie 9). Zyxin recruitment was consistently observed
224 in a small population of focal adhesions outside of the local activation region (Figure 5b). Surprisingly,
225 we found that zyxin also accumulated along stress fibers in the region of local activation (Figure 5c,d).
226 Given the myosin accumulation and direction of flow, this suggests that zyxin is recruited to both sites
227 of compression and extension. Paxillin, another mechanosensitive LIM domain protein that responds
228 to stress [46,47], behaved similarly to zyxin (Supplementary Figure S4).
229
230 **Zyxin is required for stress fibers to behave elastically**
231 To further explore the role of zyxin in stress fiber mechanical behavior we used mouse embryonic
232 fibroblast cells derived from zyxin$^{-/-}$ mice[48]. Despite the loss of zyxin, these cells form actin stress fibers
233 and focal adhesions and are highly contractile[49]. When we locally activated RhoA in the zyxin$^{-/-}$ cells,
234 myosin accumulated in the activation region (Figure 5e and Supplementary Movie 10). This
235 accumulation drove a contractile flow into the local activation area that was indistinguishable from
236 wild type cells. Upon stopping the GEF recruitment in zyxin$^{-/-}$ cells, cytoskeletal flow returned to pre-
237 activation rates, consistent with the reduced local contraction, but did not reverse direction (Figure 5e-
238 f,i, Supplementary Figure S5, and Supplementary Movie 10). Expression of EGFP-zyxin in this cell line
239 restored the flow reversal (Figure 5g-i, Supplementary Figure S5 and Supplementary Movie 11).
240 Together these results indicate that zyxin is required for the flow reversal occurring after local RhoA
241 activation ends.
242

243 Using the kymographs produced in the zyin$^{-/-}$ and zyxin$^{-/-}$+EGFP-zyxin cells, we again fit the data to our
244 mechanical model (Figure 5j-l, Supplementary Figure S6). For the zyxin$^{-/-}$ cells, we found the viscoelastic
245 relaxation time reduced to 1 sec, indicating that the stress fibers are predominately fluid-like at all
246 physiological time scales. Rescue of the zyxin$^{-/-}$ cells with EGFP-zyxin resulted in parameter fits that
247 were consistent with the NIH 3T3 fibroblast data. Zyxin is thus important for maintaining the
248 qualitative mechanical response of stress fibers, ensuring they are predominately elastic at ~1 hr time
249 scales.
250
251 **Discussion**
252 This study demonstrates that the mechanical behavior of adherent cells is strongly shaped by stress
253 fibers and their ability rapid force transmission and cytoskeletal architecture even in the face of
254 molecular turnover and flow. Using an optogenetic probe to locally activate RhoA via recruitment of
255 the DH domain of LARG, a RhoA specific GEF, we find that we can stimulate a local contraction in stress
256 fibers due to an increased accumulation of actin and myosin in the activation area (Figure 6, 1). This
257 local contraction causes a tension gradient and a flow towards the activation region (Figure 6, 2). The
258 flow of myosin and α-actinin increases the strain both on the interface coupling the stress fiber to the
259 adhesion and in the activation region, leading to recruitment of the mechanosensitive protein zyxin
260 (Figure 6, 3). When local activation of RhoA is stopped, the system relaxes to the pre-activation state,
261 mainly driven by elastic energy accumulated in the strained regions, and results in a cytoskeletal flow
262 of material away from the local activation region (Figure 6, 4).
263
264 This elastic behavior is dependent on zyxin. Previous reports have shown that zyxin localizes along the
265 stress fiber at the interface of the adhesion[50,51]. This positioning suggests that previously reported
266 zyxin mediated stress fiber repair mechanisms[46,49] are also occurring at the adhesion interface as actin
267 is assembled and is incorporated into the stress fiber while under tension. The localization of zyxin to
268 sites of compression, however, is novel. While it is known that the LIM domain of zyxin is sufficient for
269 localization[52], the exact mechanism through which zyxin recognizes sites of strain remains unknown.
270

271 These data further illustrate that RhoA activity and its downstream effectors are tightly regulated by
272 the cell. We see no evidence that RhoA activation alone leads to *de novo* stress fiber formation or
273 adhesion maturation. Instead these processes likely result from concurrent changes in cytoskeletal
274 architecture[35,53]. More interestingly, the data suggest cells regulate total RhoA activity to maintain a
275 constant homeostasis[36-38]. Specifically, the relaxation kinetics of the downstream effectors match the
276 kinetics of the optogenetic probe[28], thus indicating that there is no positive feedback loop whereby
277 production of RhoA•GTP alone is sufficient to promote further activation of RhoA. To sustain a given
278 contractile state, therefore, the cell must actively regulate and maintain a specific RhoA•GTP
279 concentration.
280
281 By using an optogenetic approach to perturb the local mechanical balance within the cell, we were
282 able probe the material properties of the cytoskeleton in ways previously inaccessible. Given that
283 typical turnover rates for proteins in the cytoskeleton are on the order of tens of seconds[15], it is
284 surprising that the cell behaves elastically on timescales of ~1 hour. The viscous behavior of cells is
285 typically associated with irreversible changes brought on through remodeling and dynamic activity of
286 proteins (e.g. cytoskeletal remodeling during migration)[21,54,55]. Conversely, elasticity has typically been
287 used to describe cellular material properties that ignore the dynamic activity of the components[36,56,57].
288 The finding that cells can maintain their elasticity and their dynamic activity simultaneously has
289 exciting implications for interpreting the underlying physics of active materials. The fact that this
290 behavior can be controlled by the activity of a single protein suggests intriguing potential mechanisms
291 to regulate cell mechanics during morphogenesis and development.

292 **Methods**

293 **Cell culture and transfection**

294 NIH 3T3 fibroblasts (American Type Culture Collection, Manassas, VA) were cultured in DMEM media
295 (Mediatech, Herndon, VA) and supplemented with 10% FBS (HyClone; ThermoFisher Scientific,
296 Hampton, NH), 2 mM L-glutamine (Invitrogen, Caarlsbad, CA) and penicillin-streptomycin (Invitrogen).
297 Zyxin$^{-/-}$ and zyxin$^{-/-}$+EGFP-zyxin Mouse Embryonic Fibroblast cells were a gift of Mary Beckerle's lab
298 (University of Utah, Salt Lake City, UT) and cultured similarly to the NIH 3T3 fibroblasts[49]. All cells were
299 transiently transfected via electroporation 24 hrs prior to experiment using a Neon Transfection
300 system (ThermoFisher Scientific). Following transfection, cells were plated on glass coverslips and
301 imaged the next day.

302

303 **Drug treatments**

304 Cells were treated with either the 10 µM SMIFH2 a pan-formin inhibitor[31] or 1µM of Y-27632 which
305 inhibits ROCK (ThermoFisher Scientific), for at least 30 minutes prior to imaging.

306

307 **Plasmids**

308 The optogenetic membrane tether consisting of Stargazin-GFP-LOVpep and prGEF constructs used are
309 previously described (Wagner 2016). prGEF-YFP was constructed in an identical manner to prGEF with
310 YFP replacing mCherry. This construct was used in experiments where the effects on various
311 downstream markers were visualized. To examine effects on the actin and myosin networks, we used
312 mApple-Actin and mApple-MLC constructs (gifts from M Davidson, University of Florida, Gainesville FL),
313 mCherry-Vinculin (gift from V Weaver, University of California at San Francisco, San Francisco, CA) and
314 mCherry-zyxin (gift from M Beckerle, University of Utah, Salt Lake City, UT).

315

316 **Live cell imaging**

317 Glass coverslips were placed in a Chamlide magnetic chamber (Live Cell Instrument, Seoul, Korea) in
318 culture media supplemented with 10 mM HEPES and 30µL/mL Oxyrase (Oxyrase Inc., Mansfield, OH)
319 and maintained at 37˚C. Cells were imaged on an inverted Nikon Ti-E microscope (Nikon, Melville, NY)
320 with a Yokogawa CSU-X confocal scanhead (Yokogawa Electric, Tokyo, Japan), and laser merge module

321 containing 491nm, 561nm, and 642nm laser lines (Spectral Applied Research, Ontario, Canada). Images
322 were collected on either a CoolSNAP HQ2 CCD (Roper Scientific, Trenton, NJ) or Zyla 4.2 sCMOS
323 Camera (Andor, Belfast, United Kingdom). Local recruitment using the optogenetic probe was
324 performed using a 405 nM laser coupled to a Mosaic digital micromirror device (Andor). Images were
325 collected using a 60x 1.49 NA ApoTIRF oil immersion objective (Nikon). All hardware was controlled
326 using MetaMorph Automation and Image Analysis Software (Molecular Devices, Sunnyvale, CA).
327
328 Unless otherwise stated, cells were imaged in the 561 channel every 20 s for 45 min, with the first 15
329 min used to determine the steady state of the system, the second 15 min to perform local recruitment,
330 and the final 15 min to record any recovery. During recruitment a local region drawn in MetaMorph
331 was illuminated by the 405nm laser for 960 ms at a power < 1 μJ/s immediately prior to the acquisition
332 of each 561 image.
333
334 **Local recruitment analysis**
335 All data analysis was performed using MATLAB (Mathworks, Natick, MA). Regions of interest (ROIs)
336 were drawn to calculate the average intensity in the local recruitment region, a control area within the
337 cell but far away from the recruitment area, and a background area outside of the cell. The average
338 background intensity was subtracted from the control region and this curve was used to determine a
339 photobleaching correction. The photobleaching correction was then applied to the background
340 subtracted average intensity in the local recruitment region and normalized to the average value of the
341 first 15 min of the data.
342
343 **Focal adhesion analysis**
344 Images were thresholded and segmented to create binary masks using MATLAB. Adhesion masks were
345 filtered to exclude adhesions smaller than 0.4 μm^2 due to the inability to segment them consistently.
346 The binary mask was then used to calculate the total number and average fluorescence intensity of
347 adhesions in each frame. These masks were also used to calculate the average stress under the
348 adhesions. To calculate the percentage of adhesions which increased in intensity or stress during
349 activation, we compared the maximum intensity of the adhesion during activation to the intensity

350 immediately prior to activation. Adhesions were considered to have shown an increase in either
351 intensity or stress if the magnitude of the increase was greater than 10%.
352
353 **Kymograph and local displacement analysis**
354 Kymographs were created in MATLAB by drawing lines along stress fibers and averaging across a width
355 of 9 pixels. Local displacement was determined by locating a feature 5μm from the edge of the
356 activation zone in a kymograph immediately prior to activation. The location of this feature was then
357 tracked and recorded following the 15 minute period of activation, and then again following 15
358 minutes of relaxation.
359
360 **Cytoskeletal flow analysis**
361 Images were first corrected for bleaching and then filtered with a 3D Gaussian filter to remove noise.
362 Flow fields were calculated using an implementation of the Brox et al. optical flow algorithm[39,40] that
363 ensures spatial and temporal smoothness. Flow field kymographs were generated by projecting the
364 flow vectors onto the line defining the kymograph. To compare the direction of flow with the
365 organization of the cytoskeleton, the local orientation of actin fibers was extracted from the structure
366 tensor[58].
367
368 **α-actinin spacing analysis**
369 Kymographs were drawn as above. For each timepoint in the kymograph, local peaks in the linescan
370 were determined. Peaks were then connected to create tracks across the kymograph. Local velocity
371 was determined by isolating the section of the track during the activation period and fitting the
372 trajectory to a straight line. The fitted slope was taken as the velocity.
373
374 **Traction force microscopy**
375 Traction force microscopy was performed as described previously[33,34,36]. Briefly, polyacrylamide gels
376 embedded with 40-nm fluorescent microspheres (Invitrogen) were polymerized on activated glass
377 coverslips. The shear modulus of the gels used in these experiments was 8.6 kPa. Following
378 polymerization gels were washed with PBS and crosslinked with the extracellular matrix protein

379 fibronectin (Millipore, Billerica, MA) using the photoactivatable crosslinker sulfo-sanpah (Thermo
380 Fisher Scientific). Cells were plated and allowed to spread for at least 4 hours prior to imaging as
381 described above.
382
383 Following imaging, cells were removed from the substrate using 0.5% sodium dodecyl sulfate and a
384 reference image of the fluorescent beads in the unstrained substrate was taken. The image stack was
385 then aligned to correct for drift and compared to the reference image using particle imaging
386 velocimetry to create a displacement field with a grid spacing of 0.86 µm. Displacement vectors were
387 filtered and interpolated using the Kriging interpolation method. Traction stresses were reconstructed
388 via Fourier Transform Traction Cytometry[33,59], with a regularization parameter chosen by minimizing
389 the L2 curve[34]. The strain energy was calculated as one half the integral of the traction stress field
390 dotted into the displacement field[36].
391
392 **Statistical analysis**
393 All experiments were repeated a minimum of 3 times. Cells presented in figures are representative
394 samples of the population behavior. Box plots represent the 25th, 50th and 75th percentiles of the data.
395 Whiskers on the boxplot extend to the most extreme data points not considered outliers. Error bars
396 represent the standard deviation, except where noted otherwise. Statistical significance was
397 determined using independent two-sample Student's *t* tests of the mean to compare groups of data.
398 Statistical significance is indicated by asterisks: (*) represents a p-value < 0.05; (**) represents a p-
399 value < 0.01.
400

401 References:

402 1. Lecuit, T., Lenne, P.-F. & Munro, E. Force generation, transmission, and integration during cell
403 and tissue morphogenesis. *Annu Rev Cell Dev Biol* **27,** 157–184 (2011).
404 2. Paluch, E. & Heisenberg, C.-P. Biology and Physics of Cell Shape Changes in Development.
405 *Current Biology* **19,** R790–R799 (2009).
406 3. Iskratsch, T., Wolfenson, H. & Sheetz, M. P. Appreciating force and shape—the rise of
407 mechanotransduction in cell biology. *Nat Rev Mol Cell Biol* **15,** 825–833 (2014).
408 4. Murrell, M., Oakes, P. W., Lenz, M. & Gardel, M. L. Forcing cells into shape: the mechanics of
409 actomyosin contractility. *Nat Rev Mol Cell Biol* **16,** 486–498 (2015).
410 5. Martin, A. C., Gelbart, M., Fernandez-Gonzalez, R., Kaschube, M. & Wieschaus, E. F. Integration
411 of contractile forces during tissue invagination. *J Cell Biol* **188,** 735–749 (2010).
412 6. Wagner, E. & Glotzer, M. Local RhoA activation induces cytokinetic furrows independent of
413 spindle position and cell cycle stage. *J Cell Biol* **213,** 641–649 (2016).
414 7. Melvin, A. T., Welf, E. S., Wang, Y., Irvine, D. J. & Haugh, J. M. In chemotaxing fibroblasts, both
415 high-fidelity and weakly biased cell movements track the localization of PI3K signaling. *Biophys J*
416 **100,** 1893–1901 (2011).
417 8. Plotnikov, S. V. & Waterman, C. M. Guiding cell migration by tugging. *Curr Opin Cell Biol* **25,** 619–
418 626 (2013).
419 9. McBeath, R., Pirone, D. M., Nelson, C. M., Bhadriraju, K. & Chen, C. S. Cell shape, cytoskeletal
420 tension, and RhoA regulate stem cell lineage commitment. *Dev Cell* **6,** 483–495 (2004).
421 10. Wang, A. *et al.* Nonmuscle myosin II isoform and domain specificity during early mouse
422 development. *Proc. Natl. Acad. Sci. U.S.A.* **107,** 14645–14650 (2010).
423 11. Müller, T. *et al.* Non-muscle myosin IIA is required for the development of the zebrafish
424 glomerulus. *Kidney Int.* **80,** 1055–1063 (2011).
425 12. Schwarz, U. S. & Gardel, M. L. United we stand - integrating the actin cytoskeleton and cell-
426 matrix adhesions in cellular mechanotransduction. *J Cell Sci* **125,** 3051–3060 (2012).
427 13. Blanchoin, L., Boujemaa-Paterski, R., Sykes, C. & Plastino, J. Actin dynamics, architecture, and
428 mechanics in cell motility. *Physiol Rev* **94,** 235–263 (2014).
429 14. Fletcher, D. A. & Mullins, R. D. Cell mechanics and the cytoskeleton. *Nature* **463,** 485–492
430 (2010).
431 15. Hotulainen, P. & Lappalainen, P. Stress fibers are generated by two distinct actin assembly
432 mechanisms in motile cells. *J Cell Biol* **173,** 383–394 (2006).
433 16. Devreotes, P. & Horwitz, A. R. Signaling Networks that Regulate Cell Migration. *Cold Spring Harb*
434 *Perspect Biol* **7,** a005959 (2015).
435 17. Gardel, M. L., Schneider, I. C., Aratyn-Schaus, Y. & Waterman, C. M. Mechanical integration of
436 actin and adhesion dynamics in cell migration. *Annu Rev Cell Dev Biol* **26,** 315–333 (2010).
437 18. Hoffman, B. D. & Crocker, J. C. Cell mechanics: dissecting the physical responses of cells to force.
438 *Annu Rev Biomed Eng* **11,** 259–288 (2009).
439 19. Stricker, J., Falzone, T. & Gardel, M. L. Mechanics of the F-actin cytoskeleton. *J Biomech* **43,** 9–14
440 (2010).
441 20. Zhu, C., Bao, G. & Wang, N. Cell mechanics: mechanical response, cell adhesion, and molecular
442 deformation. *Annu Rev Biomed Eng* **2,** 189–226 (2000).
443 21. Prost, J., Julicher, F. & Joanny, J.-F. Active gel physics. *Nature Physics* **11,** 111–117 (2015).

444 22. Schwarz, U. S. & Safran, S. A. Physics of adherent cells. *Rev Mod Phys* **85,** 1327 (2013).
445 23. Broedersz, C. P. & Mackintosh, F. C. Modeling semiflexible polymer networks. *Rev Mod Phys* **86,**
446 995 (2014).
447 24. Ridley, A. J. & Hall, A. The small GTP-binding protein rho regulates the assembly of focal
448 adhesions and actin stress fibers in response to growth factors. *Cell* **70,** 389–399 (1992).
449 25. Chrzanowska-Wodnicka, M. & Burridge, K. Rho-stimulated contractility drives the formation of
450 stress fibers and focal adhesions. *J Cell Biol* **133,** 1403–1415 (1996).
451 26. Machacek, M. *et al.* Coordination of Rho GTPase activities during cell protrusion. *Nature* **461,**
452 99–103 (2009).
453 27. Pertz, O., Hodgson, L., Klemke, R. L. & Hahn, K. M. Spatiotemporal dynamics of RhoA activity in
454 migrating cells. *Nature* **440,** 1069–1072 (2006).
455 28. Strickland, D. *et al.* TULIPs: tunable, light-controlled interacting protein tags for cell biology. *Nat*
456 *Methods* **9,** 379–384 (2012).
457 29. Guilluy, C. *et al.* The Rho GEFs LARG and GEF-H1 regulate the mechanical response to force on
458 integrins. *Nat Cell Biol* **13,** 722–727 (2011).
459 30. Jaiswal, M. *et al.* Mechanistic insights into specificity, activity, and regulatory elements of the
460 regulator of G-protein signaling (RGS)-containing Rho-specific guanine nucleotide exchange
461 factors (GEFs) p115, PDZ-RhoGEF (PRG), and leukemia-associated RhoGEF (LARG). *J Biol Chem*
462 **286,** 18202–18212 (2011).
463 31. Rizvi, S. A. *et al.* Identification and characterization of a small molecule inhibitor of formin-
464 mediated actin assembly. *Chem Biol* **16,** 1158–1168 (2009).
465 32. Balaban, N. Q. *et al.* Force and focal adhesion assembly: a close relationship studied using elastic
466 micropatterned substrates. *Nat Cell Biol* **3,** 466–472 (2001).
467 33. Sabass, B., Gardel, M., Waterman, C. M. & Schwarz, U. S. High resolution traction force
468 microscopy based on experimental and computational advances. *Biophys J* **94,** 207–220 (2008).
469 34. Soiné, J. R. D. *et al.* Model-based Traction Force Microscopy Reveals Differential Tension in
470 Cellular Actin Bundles. *PLoS Comput Biol* **11,** e1004076 (2015).
471 35. Oakes, P. W., Beckham, Y., Stricker, J. & Gardel, M. L. Tension is required but not sufficient for
472 focal adhesion maturation without a stress fiber template. *J Cell Biol* **196,** 363–374 (2012).
473 36. Oakes, P. W., Banerjee, S., Marchetti, M. C. & Gardel, M. L. Geometry regulates traction stresses
474 in adherent cells. *Biophys J* **107,** 825–833 (2014).
475 37. Ingber, D. E. Tensegrity I. Cell structure and hierarchical systems biology. *J Cell Sci* **116,** 1157–
476 1173 (2003).
477 38. Webster, K. D., Ng, W. P. & Fletcher, D. A. Tensional Homeostasis in Single Fibroblasts. *Biophys J*
478 **107,** 146–155 (2014).
479 39. Brox, T., Bruhn, A., Papenberg, N. & Weickert, J. in *Computer Vision - ECCV 2004* 25–36 (Springer
480 Berlin Heidelberg, 2004). doi:10.1007/978-3-540-24673-2_3
481 40. Sánchez, J., Monzón, N. & Salgado, A. Robust Optical Flow Estimation. *Image Processing On Line*
482 **3,** 252–270 (2013).
483 41. Cai, Y. *et al.* Cytoskeletal coherence requires myosin-IIA contractility. *J Cell Sci* **123,** 413–423
484 (2010).
485 42. Xu, K., Babcock, H. P. & Zhuang, X. Dual-objective STORM reveals three-dimensional filament
486 organization in the actin cytoskeleton. *Nat Methods* **9,** 185–188 (2012).
487 43. Colombelli, J. *et al.* Mechanosensing in actin stress fibers revealed by a close correlation

488 between force and protein localization. *J Cell Sci* **122,** 1665–1679 (2009).
489 44. Yoshigi, M., Hoffman, L. M., Jensen, C. C., Yost, H. J. & Beckerle, M. C. Mechanical force mobilizes
490 zyxin from focal adhesions to actin filaments and regulates cytoskeletal reinforcement. *J Cell Biol*
491 **171,** 209–215 (2005).
492 45. Zaidel-Bar, R., Ballestrem, C., Kam, Z. & Geiger, B. Early molecular events in the assembly of
493 matrix adhesions at the leading edge of migrating cells. *J Cell Sci* **116,** 4605–4613 (2003).
494 46. Smith, M. A. *et al.* LIM domains target actin regulators paxillin and zyxin to sites of stress fiber
495 strain. *PLoS ONE* **8,** e69378 (2013).
496 47. Smith, M. A., Hoffman, L. M. & Beckerle, M. C. LIM proteins in actin cytoskeleton
497 mechanoresponse. *Trends Cell Biol* **24,** 575–583 (2014).
498 48. Hoffman, L. M. *et al.* Genetic ablation of zyxin causes Mena/VASP mislocalization, increased
499 motility, and deficits in actin remodeling. *J Cell Biol* **172,** 771–782 (2006).
500 49. Smith, M. A. *et al.* A zyxin-mediated mechanism for actin stress fiber maintenance and repair.
501 *Dev Cell* **19,** 365–376 (2010).
502 50. Guo, W.-H. & Wang, Y.-L. Retrograde fluxes of focal adhesion proteins in response to cell
503 migration and mechanical signals. *Mol Biol Cell* **18,** 4519–4527 (2007).
504 51. Kanchanawong, P. *et al.* Nanoscale architecture of integrin-based cell adhesions. *Nature* **468,**
505 580–584 (2010).
506 52. Uemura, A., Nguyen, T.-N., Steele, A. N. & Yamada, S. The LIM domain of zyxin is sufficient for
507 force-induced accumulation of zyxin during cell migration. *Biophys J* **101,** 1069–1075 (2011).
508 53. Aratyn-Schaus, Y., Oakes, P. W. & Gardel, M. L. Dynamic and structural signatures of lamellar
509 actomyosin force generation. *Mol Biol Cell* **22,** 1330–1339 (2011).
510 54. Callan-Jones, A. C. & Voituriez, R. Active gel model of amoeboid cell motility. *New J Phys* **15,**
511 025022 (2013).
512 55. Besser, A. & Schwarz, U. S. Coupling biochemistry and mechanics in cell adhesion: a model for
513 inhomogeneous stress fiber contraction. *New J Phys* **9,** 425 (2007).
514 56. Edwards, C. M. & Schwarz, U. S. Force localization in contracting cell layers. *Phys Rev Lett* **107,**
515 128101 (2011).
516 57. Farsad, M. & Vernerey, F. J. An XFEM-based numerical strategy to model mechanical
517 interactions between biological cells and a deformable substrate. *Int J Numer Meth Engng* **92,**
518 238–267 (2012).
519 58. Weichsel, J., Urban, E., Small, J. V. & Schwarz, U. S. Reconstructing the orientation distribution of
520 actin filaments in the lamellipodium of migrating keratocytes from electron microscopy
521 tomography data. *Cytometry A* **81,** 496–507 (2012).
522 59. Butler, J. P., Tolić-Nørrelykke, I. M., Fabry, B. & Fredberg, J. J. Traction fields, moments, and
523 strain energy that cells exert on their surroundings. *Am J Physiol Cell Physiol* **282,** C595–605
524 (2002).
525

526

527 **Figure Captions**

528 **Figure 1**

529 RhoA activity can be spatiotemporally controlled via an optogenetic probe. (**a**) Spatiotemporal control
530 of RhoA activity is achieved using an optogenetic probe to recruit the RhoA specific GEF LARG to the
531 plasma membrane. A LOVpep molecule is anchored to the membrane via fusion to the transmembrane
532 protein Stargazin, while a protein consisting of tandem PDZ domains fused to the DH domain of LARG
533 (prGEF) is distributed throughout the cytosol. Upon stimulation with 405nm light, the LOVpep
534 undergoes a conformational change exposing a high-affinity binding site which drives the prGEF to the
535 membrane where it can activate RhoA. When the activating light is removed, the LOVpep undergoes a
536 thermodynamically driven refolding halting further recruitment of prGEF. (**b**) The RhoA signaling
537 pathway. RhoA*GTP activates both Dia and ROCK, which in turn promote actin polymerization and
538 myosin II activation, respectively. (**c**) Representative images of a 3T3 fibroblast expressing an mCherry-
539 tagged version of prGEF. Upon local activation (top row – orange box) mCherry-prGEF rapidly
540 accumulates in the activation region. Removal of the activating light (bottom row) results in the
541 accumulated mCherry-prGEF dispersing back into the cytosol. (**d**) Quantification of the local intensity
542 increase of mCherry-prGEF in the activation region of the cell shown in **c**. The activation period is
543 indicated by a blue background. (**e-f**) Representative images of cells expressing either mApple-Actin (**e**)
544 or mApple-Myosin Light Chain (**f**) prior to activation, following 15 minutes of activation in the region
545 indicated, and following 15 minutes of relaxation. Both actin and myosin exhibit increases in intensity
546 in the local region of activation. (**g**) Quantification of the local intensity increase of actin and myosin
547 from the cells in **e-f**. Both signals begin increasing immediately upon RhoA activation, and dissipate as
548 soon as the activating light is switched off. (**h**) Mean maximum intensity fold-increase of actin or
549 myosin in regions of activation in control cells, or cells treated with 10 µM SMIFH2 (Dia inhibitor) or
550 1µM Y-27632 (ROCK inhibitor). Inhibition of either Dia or ROCK results in reduced average increases in
551 local intensity during RhoA activation. Time is min:sec.

552

553 **Figure 2**

554 Increased RhoA activity leads to increased cell contractility. (**a**) A cell expressing mCherry-Vinculin is
555 shown prior to activation, after 15 minutes of activation, and after 15 minutes of relaxation. The

556 activation region is indicated by the orange box. (**b**) The corresponding traction stress maps for the
557 time series shown in **a**. (**c**) A plot showing the strain energy versus time and the number of focal
558 adhesions versus time, with the activation period indicated by the blue background. The strain energy
559 begins to increase immediately upon activation, and begins to relax as soon as the activating light is
560 removed. In contrast, the number of focal adhesions remains relatively constant and does not respond
561 to the local increase in RhoA activity. (**d**) The average stress and fluorescence intensity of a
562 representative adhesion marked by the white box in **a**. Kymographs were generated by drawing a line
563 along the long axis of the adhesion. The activation period is indicated by the orange bar above the
564 kymograph. (**e**) A sequence of traction maps from a cell exposed to a series of activations in regions of
565 different size. Time is hr:min:sec. (**f**) A plot of the experimental (black line) and theoretical (red line)
566 strain energy vs time for the cell shown in **e**. The contractile response of the cell is proportional to the
567 size of the activation region and retreats to a baseline value following each activation period. (**g**) A
568 cartoon of the continuum model used to describe the cell in **e**. The model consists of a contractile
569 element (σ_m) in series with a viscous (η) and an elastic element (k), connected via a frictional elements
570 (γ) to an elastic substrate (k_M).
571
572 **Figure 3**
573 Stress fibers direct contractile flow. (**a**) Fluorescence time series of a cell expressing mApple-MLC
574 shown prior and after two separate periods of activation (orange boxes). (**b**) Flow fields of myosin
575 calculated from the images in **a**. Flow is always directed along the direction of the stress fibers. (**c**) A
576 two dimensional model of the cell was created using a triangular mesh of viscoelastic-cables (k, η)
577 connected at vertices viscously coupled (γ) to the environment. Stress fibers (blue line) consisting of
578 contractile (σ_m), viscous (η_{SF}) and elastic elements (k_{SF}) were embedded in the network. Using a
579 simplified rectangular cell with this network, local RhoA activation could be simulated by activating
580 force dipoles in network links in a region in the center of the cell. (**d**) To calibrate the 2D discrete
581 model, the average flow (white box in **c**), was measured and compared to the 1D continuum model
582 presented above. (**e-f**) The 2D discrete model was used to explore two contractile scenarios: (**e**)
583 contractile stress fibers (blue) embedded in a contractile mesh (grey); and (**f**) contractile stress fibers
584 embedded in a non-contractile background. If both the stress fibers and mesh are contractile, a

585 transverse contraction pinches together the stress fibers. If only the stress fibers contract, the flow
586 profile is restricted to the orientation of the fibers, mimicking the experimental results.
587
588 **Figure 4**
589 Stress fibers behave elastically. (**a**) Image showing a cell labeled with mApple-MLC. The activation
590 regions are indicated by the orange boxes. (**b**) A kymograph drawn along the stress fiber (green line in
591 **a**). During activation periods myosin flows towards the activation regions. (**c**) A kymograph created
592 from the same region as **b** using the flow maps determined previously. Flow was projected onto the
593 stress fiber and color coded to indicate speed and direction. This flow map illustrates that during
594 relaxation periods, myosin flow reverses direction away from the activation periods. (**d**) A
595 quantification of displacement of stress fibers during contraction and relaxation. Puncta ~5 µm from
596 the activation zone were tracked and measured following 15 minutes of activation, and again following
597 15 min of relaxation. Puncta translated about 3 µm from their original position, and relaxed to ~1 µm
598 from their original position elastically. The relaxation response could be further broken into two
599 groups, one with a strong reversal (~80% of their original position) and one with a weak reversal (~25%
600 of their original position). (**e**) A cell transfected with mApple-α-actinin. The activation area is indicated
601 by the orange box. (**f**) A kymograph drawn along the direction indicated in **e**, overlain with tracks of the
602 individual α-actinin puncta during activation. (**g**) The velocity of individual puncta along the stress fiber
603 is measured from the slope of the tracks and plotted against the distance from the activation region.
604 Adjacent puncta all move at approximately the same speed. Sudden changes in velocity (blue
605 arrowhead) correlate with what appear to be site of mechanical failure along the stress fiber and the
606 appearance of new puncta. The black line represents the stress fiber from **f**, while the grey lines are
607 other stress fibers from the same cell. (**h**) A representative kymograph is fit to both the 1D continuum
608 and 2D discrete models. Both models are able to recapitulate the flow patterns seen experimentally.
609
610 **Figure 5**
611 Zyxin accumulates at sites of strain on stress fibers during local RhoA activation. (**a**) A NIH 3T3
612 expressing mCherry-zyxin. The activation region is indicated by the orange box. (**b**) A kymograph of a
613 representative adhesion marked by the white box in **a**. (**c**) The average intensity of zyxin in the

activation region. (**d**) A kymograph illustrating the local zyxin accumulation during activation along the green line shown in **a**. (**e**) A zyxin$^{(-/-)}$ MEF expressing mApple-MLC before activation, at peak activation, and following relaxation. Myosin accumulates as in 3T3s. (**f**) A kymograph of myosin intensity and flow speed drawn along the green line indicated in **e**. Zyxin$^{(-/-)}$ MEFS exhibit little to no elastic flow reversal. (**g**) A zyxin$^{(-/-)}$ MEF rescued with EGFP-zyxin and expressing mApple-MLC, during an activation sequence. (**h**) A kymograph of myosin and flow illustrating a strong elastic flow reversal along the line drawn in **g.** (**i**) Displacement analysis of the zyxin$^{(-/-)}$ and zyxin$^{(-/-)}$+EGFP-zyxin MEFs. Without zyxin, cells do not exhibit an elastic response. (**j**) A kymograph representing the average fit of the continuum model to the zyxin$^{(-/-)}$ data. (**k**) A kymograph representing the average fit of the continuum model to the zyxin$^{(-/-)}$+EGFP-zyxin data. (**l**) The elastic (E) and viscous (η) parameters found from fitting the experimental kymographs to the continuum model. Without zyxin, the elasticity increases and the viscosity decreases.

Figure 6

Molecular and mechanical models of local RhoA activation in stress fibers. Molecular model: (1) Local recruitment of prGEF leads to activation of RhoA and accumulation of actin and myosin. The local increase in actin and myosin in turn stimulates a local contraction in the stress fiber. (2) The increased local contractility induces a flow of myosin and α-actinin along the stress fiber towards the activation region. (3) Increased flow induces higher strain at both the interface coupling the stress fiber to the focal adhesion and the activation region, resulting in recruitment of the mechanosensitive protein zyxin. (4) When local activation of RhoA stops, the flow reverses direction as the stress fiber relaxes elastically. Mechanical model: The stress fiber is represented as a contractile, viscous and elastic element connected in series. Upon local activation of RhoA, the contractile element is compressed, leading to extension of both the viscous and elastic elements. As local activation stops, the energy stored in the elastic element allows it to relax back to its original state, while the energy in the viscous element is lost.

642 **Supplementary Movie Captions**

643 **Supplementary Movie 1**

644 A NIH 3T3 fibroblast expressing mCherry-prGEF during a local activation of RhoA (from Figure 1c). Local
645 activation area is indicated by the white box. Time is in min:sec.

646

647 **Supplementary Movie 2**

648 A NIH 3T3 fibroblast expressing mApple-Actin during local activation of RhoA (from Figure 1e). Local
649 activation area is indicated by the white box. Time is in min:sec.

650

651 **Supplementary Movie 3**

652 A NIH 3T3 fibroblast expressing mApple-MLC during a local activation of RhoA (from Figure 1f). Local
653 activation area is indicated by the white box. Time is in min:sec.

654

655 **Supplementary Movie 4**

656 A NIH 3T3 fibroblast expressing mCherry-vinculin during a local activation of RhoA (from Figure 2a) and
657 the corresponding traction stress maps (from Figure 2b). Local activation is indicated by the white box.
658 Time is in min:sec.

659

660 **Supplementary Movie 5**

661 Traction stress maps of a NIH 3T3 fibroblast during a series of local RhoA activations (from Figure 2e).
662 Local activation is indicated by white boxes. Time is in hr:min:sec.

663

664 **Supplementary Movie 6**

665 A NIH 3T3 fibroblast expressing mApple-MLC during a local activation of RhoA and the corresponding
666 cytoskeletal flow maps (from Figure 3a,b). Local activation is indicated by white boxes. Time is in
667 hr:min:sec.

668

669

670

671 **Supplementary Movie 7**

672 A NIH 3T3 fibroblast expressing mApple-MLC during 3 sequential local activations of RhoA. Each
673 activation is the same area but of a different geometry. Local activation is indicated by white boxes.
674 Time is in hr:min:sec.

675

676 **Supplementary Movie 8**

677 A NIH 3T3 fibroblast expressing mApple-α-actinin during a local activation of RhoA (from Figure 4e).
678 Local activation is indicated by white boxes. Time is in min:sec.

679

680 **Supplementary Movie 9**

681 A NIH 3T3 fibroblast expressing mCherry-Zyxin during a local activation of RhoA (from Figure 5a). Local
682 activation is indicated by white boxes. Time is in min:sec.

683

684 **Supplementary Movie 10**

685 A zyxin$^{(-/-)}$ Mouse Embryonic Fibroblast expressing mApple-MLC during a local activation of RhoA (from
686 Figure 5e). Local activation is indicated by white boxes. Time is in min:sec.

687

688 **Supplementary Movie 11**

689 A zyxin$^{(-/-)}$+EGFP-zyxin Mouse Embryonic Fibroblast expressing mApple-MLC during a local activation of
690 RhoA (from Figure 5g). Local activation is indicated by white boxes. Time is in min:sec.

691

Figure 1

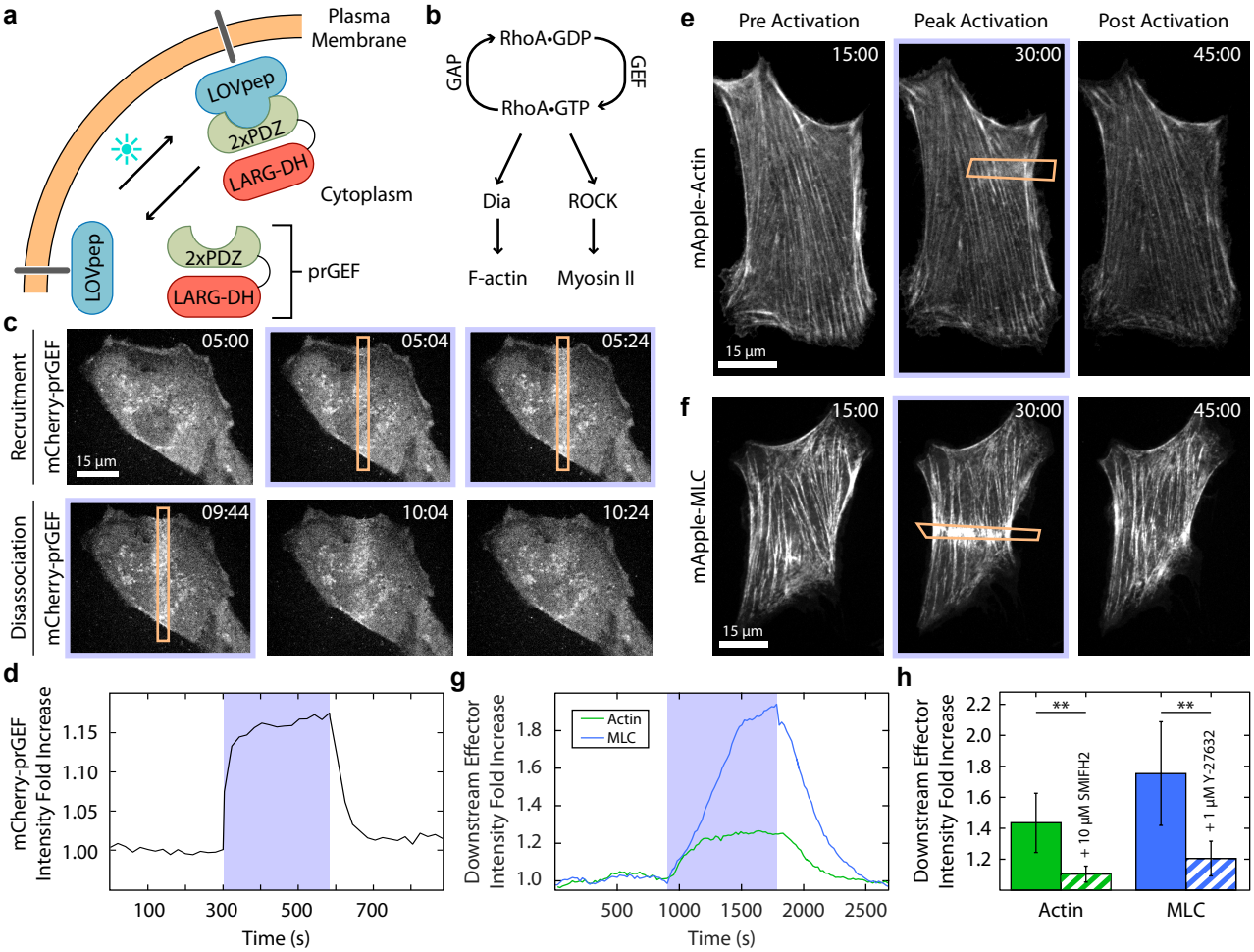
a
Plasma Membrane
LOVpep
2xPDZ
LARG-DH
Cytoplasm
LOVpep
2xPDZ
LARG-DH
prGEF
b
RhoA•GDP
GAP
GEF
RhoA•GTP
Dia
ROCK
F-actin
Myosin II
c
Recruitment
mCherry-prGEF
05:00
05:04
05:24
15 µm
Disassociation
mCherry-prGEF
09:44
10:04
10:24
e
Pre Activation
Peak Activation
Post Activation
mApple-Actin
15:00
30:00
45:00
15 µm
f
mApple-MLC
15:00
30:00
45:00
15 µm
d
mCherry-prGEF Intensity Fold Increase
1.15
1.10
1.05
1.00
100
300
500
700
Time (s)
g
Downstream Effector Intensity Fold Increase
Actin
MLC
1.8
1.6
1.4
1.2
1.0
500
1000
1500
2000
2500
Time (s)
h
Downstream Effector Intensity Fold Increase
2.2
2.0
1.8
1.6
1.4
1.2
**
**
+ 10 µM SMIFH2
+ 1 µM Y-27632
Actin
MLC

Figure 2

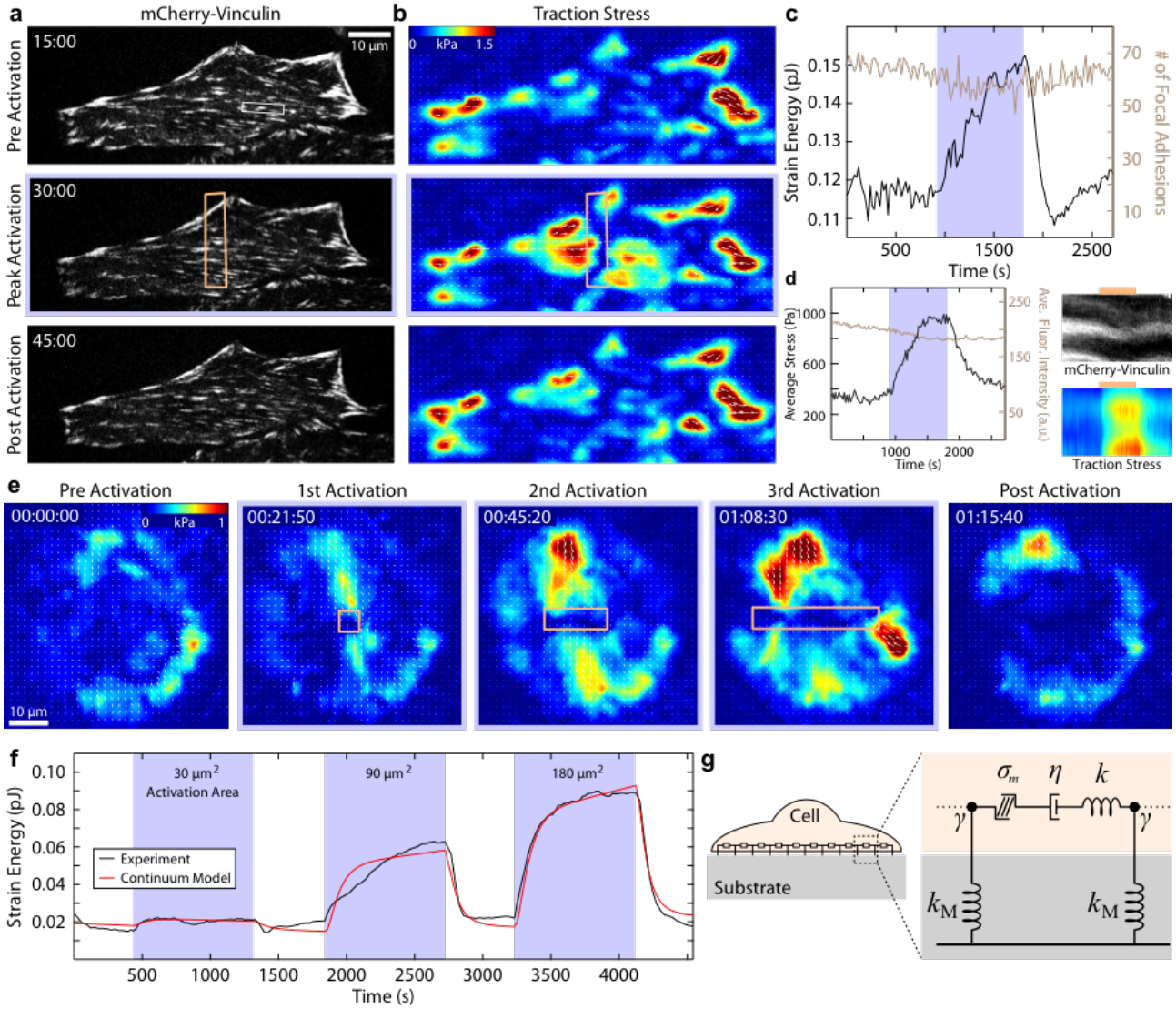
a
mCherry-Vinculin
Pre Activation
Peak Activation
Post Activation
15:00
30:00
45:00
10 µm
b
Traction Stress
0 kPa 1.5
c
Strain Energy (pJ)
# of Focal Adhesions
Time (s)
d
Average Stress (Pa)
Ave. Fluor. Intensity (a.u.)
Time (s)
mCherry-Vinculin
Traction Stress
e
Pre Activation
1st Activation
2nd Activation
3rd Activation
Post Activation
00:00:00
00:21:50
00:45:20
01:08:30
01:15:40
0 kPa 1
10 µm
f
Strain Energy (pJ)
30 µm²
Activation Area
90 µm²
180 µm²
Experiment
Continuum Model
Time (s)
g
Cell
Substrate

Figure 3

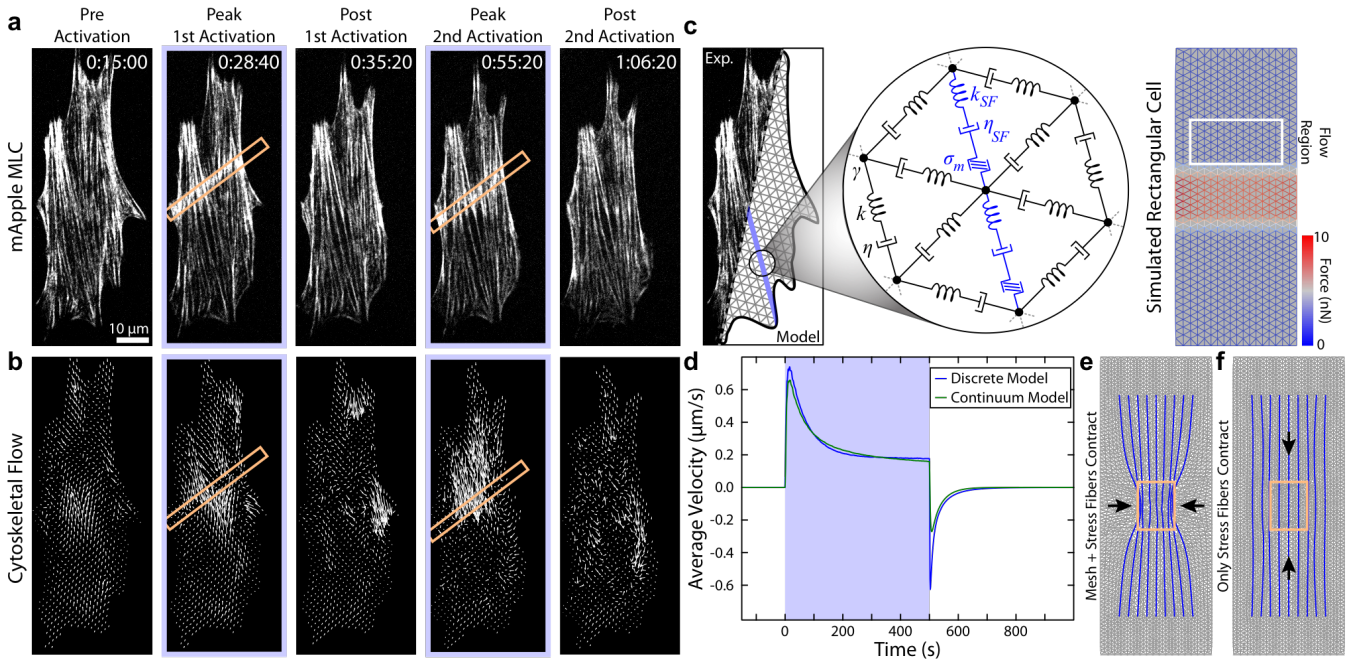
a
Pre Activation
Peak 1st Activation
Post 1st Activation
Peak 2nd Activation
Post 2nd Activation
0:15:00
0:28:40
0:35:20
0:55:20
1:06:20
mApple MLC
10 µm
b
Cytoskeletal Flow
c
Exp.
Model
Simulated Rectangular Cell
Flow Region
Force (nN)
10
0
d
Discrete Model
Continuum Model
Average Velocity (µm/s)
Time (s)
e
Mesh + Stress Fibers Contract
f
Only Stress Fibers Contract

Figure 4

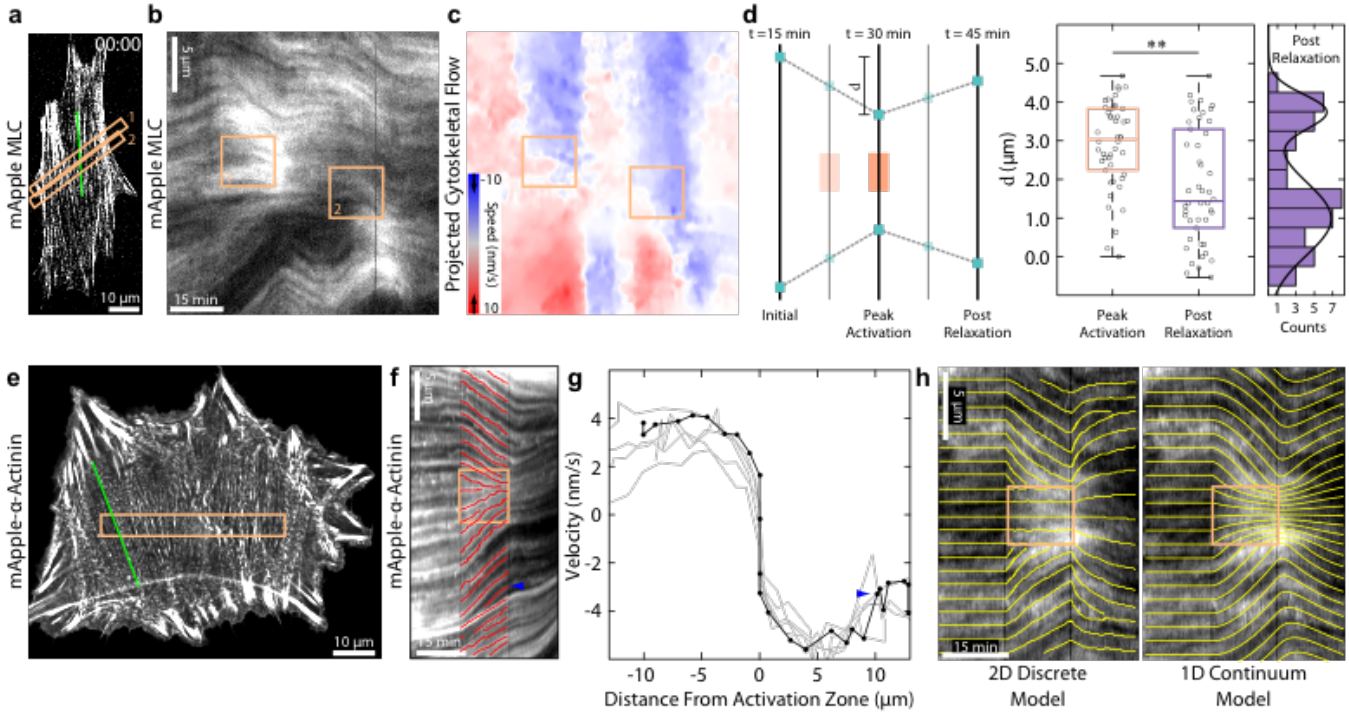
a
b
c
d
e
f
g
h
mApple MLC
00:00
10 µm
5 µm
15 min
Projected Cytoskeletal Flow
Speed (nm/s)
-10
10
t = 15 min
t = 30 min
t = 45 min
d
Initial
Peak Activation
Post Relaxation
d (µm)
5.0
4.0
3.0
2.0
1.0
0.0
**
Post Relaxation
1 3 5 7
Counts
mApple-α-Actinin
Velocity (nm/s)
4
2
0
-2
-4
-10 -5 0 5 10
Distance From Activation Zone (µm)
2D Discrete Model
1D Continuum Model

Figure 5

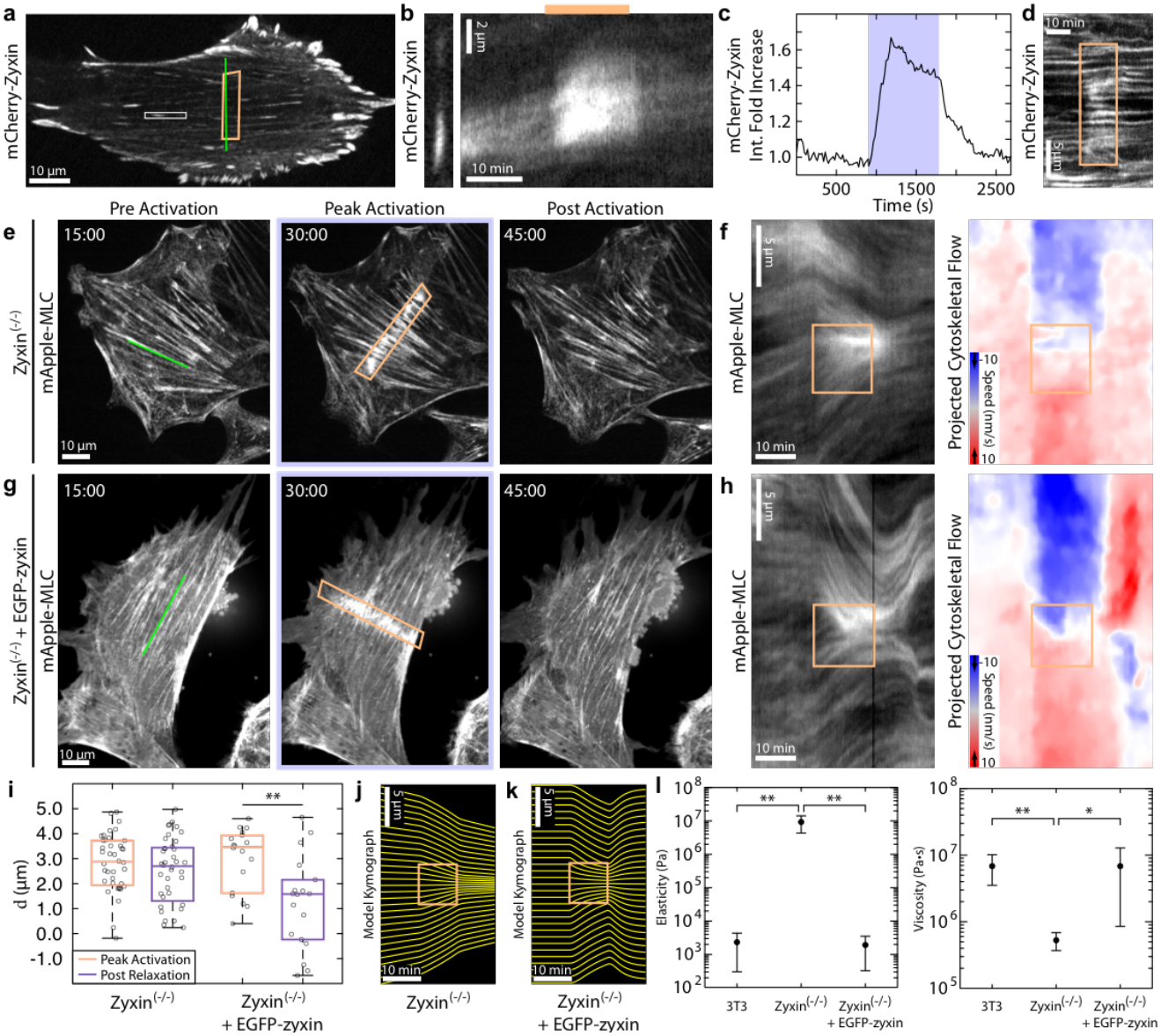
a
mCherry-Zyxin
10 µm
b
mCherry-Zyxin
2 µm
10 min
c
mCherry-Zyxin Int. Fold Increase
1.6
1.4
1.2
1.0
500
1500
2500
Time (s)
d
mCherry-Zyxin
10 min
5 µm
Pre Activation
Peak Activation
Post Activation
e
Zyxin(-/-)
mApple-MLC
15:00
30:00
45:00
10 µm
f
mApple-MLC
5 µm
10 min
Projected Cytoskeletal Flow
Speed (nm/s)
-10
10
g
Zyxin(-/-) + EGFP-zyxin
mApple-MLC
15:00
30:00
45:00
10 µm
h
mApple-MLC
5 µm
10 min
Projected Cytoskeletal Flow
Speed (nm/s)
-10
10
i
d (µm)
5.0
4.0
3.0
2.0
1.0
0.0
-1.0
**
Peak Activation
Post Relaxation
Zyxin(-/-)
Zyxin(-/-) + EGFP-zyxin
j
Model Kymograph
5 µm
10 min
Zyxin(-/-)
k
Model Kymograph
5 µm
10 min
Zyxin(-/-) + EGFP-zyxin
l
Elasticity (Pa)
**
**
3T3
Zyxin(-/-)
Zyxin(-/-) + EGFP-zyxin
Viscosity (Pa•s)
**
*
3T3
Zyxin(-/-)
Zyxin(-/-) + EGFP-zyxin

Figure 6

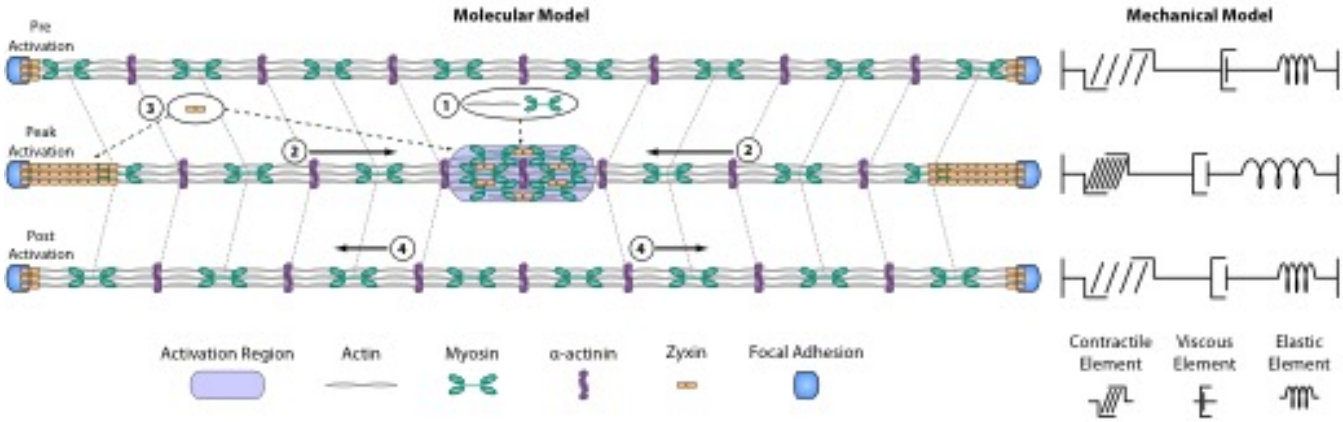
Molecular Model
Mechanical Model
Pre Activation
Peak Activation
Post Activation
Activation Region
Actin
Myosin
α-actinin
Zyxin
Focal Adhesion
Contractile Element
Viscous Element
Elastic Element